Recalibration of a Single-Valued Double Many-Body Expansion Potential Energy Surface for Ground-State HO_2 and Dynamics Calculations for the O + OH → O_2 + H Reaction

M. R. Pastrana,† L. A. M. Quintales, J. Brandão, and A. J. C. Varandas*

Departamento de Química, Universidade de Coimbra, 3049 Coimbra Codex, Portugal
(Received: January 25, 1990; In Final Form: May 2, 1990)

We report a new single-valued potential energy surface for the ground state of HO_2 from the double many-body expansion (DMBE) method. This new surface conforms with the three-body energy of recent ab initio CAS SCF/CCI calculations semiempirically corrected by the DMBE-SEC method and reproduces the most accurate estimates of the experimental dissociation energy, equilibrium geometry, and quadratic force constants for the hydroperoxyl radical. Using this new HO_2 (DMBE IV) potential energy function, exploratory dynamics calculations of the O + OH → O_2 + H reaction have also been carried out by the quasiclassical trajectory method. Thermal rate coefficients are reported for T = 250, 1250, and 2250 K that are shown to be in good agreement with the best reported measurements.

1. Introduction

Knowledge of the potential energy surface for the electronic ground state of the hydroperoxyl radical, $HO_2(\tilde{X}^2A'')$, is fundamental for studying the dynamics of the O + OH → HO^*_2 → O_2 + H reaction and its reverse, which play a prominent role in many different areas of chemistry. In particular, the reaction of atomic hydrogen with molecular oxygen is the single most important chemical reaction in combustion processes.[1-3] It is also the dominant step in many radical chain reaction mechanisms such as those occurring in the oxidation of hydrocarbons[2,4,5] and in the three-body recombination reaction H + O_2 + M → HO_2 + M (M is a bath gas).[6-8] In addition, the HO_2 radical is an important intermediate for many chemical reactions such as those involved in atmospheric chemistry,[7,9-18] stratospheric formation, and destruction of ozone[7,14,15,19-21] and in photochemical air pollution.[22-26] Moreover, this radical is significant for the formation of O_2 in interstellar clouds,[27] and it also takes part in many biological reactions.[28]

Theoretically, it is well established that the title reaction occurs without a barrier[29-32] (with respect to the infinitely separated reactants; see later) on the $HO_2(\tilde{X}^2A'')$ potential energy surface. In addition, its dynamics has been suggested[29,31-38] to be dominated by the long-range O–OH intermolecular forces. Thus, it also provides an important prototype for atom–diatom neutral reactions for which long-range forces are expected to play an important role in the dynamics of the approaching reactants.

The HO_2 radical has therefore been much studied both experimentally and theoretically, and we give a considerable list of references here. Experimentally detected in the 1950s,[39,40] there has been since then a wealth of reported spectroscopic and thermochemical information for this species.[41-60] Measurements of the thermal rate coefficient for the title reaction and its reverse over a wide range of temperatures have also been reported on many occasions.[8,61-70] Theoretically, the potential energy surface for the ground state (as well as for some excited states) of the hydroperoxyl radical has been much studied by using both ab initio[71-82] and semiempirical[36,75,83-88] methods. Moreover, there have been many dynamics calculations of the title reaction and its reverse using various potential energy surfaces and techniques. These include the quasiclassical trajectory method using the Melius–Blint[75] potential,[30,32,33,89-91] the double many-body expansion (DMBE)[87] potential energy surfaces,[32,38,92,93] and other models[32,84] several forms of adiabatic capture quantum dynamics theory using the many-body expansion (MBE)[83] potential energy surface,[29] and simple long-range electrostatic forms,[34] statistical adiabatic channel calculations using simple one-dimensional potential models,[8,35] variational transition-state theory calculations on the Melius–Blint surface,[94,95] on the Lemon–Hase[86] potential[95] and on the DMBE potential energy surfaces,[93,96] and Gorin-type transition-state theory calculations on various representations of

† Permanent address: Departamento de Química Física, Universidad de Valladolid, 47005 Valladolid, Spain.

(1) Glassman, I. *Combustion*; Academic: New York, 1977.
(2) Benson, S. W.; Nangia, P. S. *Acc. Chem. Res.* **1979**, *12*, 223.
(3) Benson, S. W. *Prog. Energy Combust. Sci.* **1981**, *7*, 125.
(4) Jachimowski, C. J. *Combust. Flame* **1974**, *23*, 233.
(5) Smoot, L. D.; Hecker, W. C.; Williams, G. A. *Combust. Flame* **1976**, *26*, 323.
(6) Troe, J.; Wagner, H. G. *Annu. Rev. Phys. Chem.* **1972**, *23*, 311.
(7) Troe, J. *Annu. Rev. Phys. Chem.* **1978**, *29*, 223.
(8) Cobos, C. J.; Hippler, H.; Troe, J. *J. Phys. Chem.* **1985**, *89*, 342.
(9) Bates, D. R.; Nicolet, M. *J. Geophys. Res.* **1950**, *55*, 301.
(10) Hunt, B. G. *J. Geophys. Res.* **1966**, *71*, 1385.
(11) Nicolet, M. *Planet. Space Sci.* **1972**, *20*, 1671.
(12) Rowland, F. S.; Molina, M. *Rev. Geophys. Space Phys.* **1975**, *13*, 1.
(13) Nicolet, M. *Rev. Geophys. Space Phys.* **1975**, *13*, 593.
(14) Kaufman, F. *Annu. Rev. Phys. Chem.* **1979**, *30*, 411.
(15) Chang, J. S.; Duewer, W. H. *Annu. Rev. Phys. Chem.* **1979**, *30*, 443.
(16) *The Stratosphere: Present and Future*; Hudson, R. D., Reed, E. I., Eds.; NASA-RP1049, 1979.
(17) Lee, Y. P.; Howard, C. J. *J. Chem. Phys.* **1982**, *77*, 756.
(18) Nicolet, M. *Adv. Chem. Phys.* **1985**, *55*, 63.
(19) Khrgian, A. Kh. *The Physics of Atmospheric Ozone*; Wiley: Chichester, 1975.
(20) Duewer, W. H.; Wuebbles, D. J.; Ellsaesser, H. W.; Chang, J. S. *J. Geophys. Res.* **1977**, *82*, 935.
(21) Nangia, P. S.; Benson, S. W. *J. Am. Chem. Soc.* **1980**, *102*, 3105.
(22) Paukert, T. T.; Johnston, H. S. *J. Chem. Phys.* **1972**, *56*, 2824.
(23) Poulet, G.; Le Bras, G.; Combourieu, J. *J. Chem. Phys.* **1978**, *69*, 767.
(24) Atkinson, R.; Darnall, K. R.; Lloyd, A. C.; Winer, A. M.; Pitts, J. N., Jr. *Adv. Photochem.* **1979**, *11*, 375.
(25) Trush, B. A. In *Pathways of Pollutants in the Atmosphere*; Royal Society: London, 1979.
(26) Leck, T. J.; Jac. Cook, E. L.; Birks, J. W. *J. Chem. Phys.* **1980**, *72*, 2364.
(27) Dalgarno, A.; Black, J. H. *Rep. Prog. Phys.* **1976**, *39*, 573.
(28) Dix, T. A.; Marnett, L. J. *J. Biol. Chem.* **1985**, *260*, 5351.
(29) Clary, D. C. *Mol. Phys.* **1984**, *53*, 3.
(30) Miller, J. A. *J. Chem. Phys.* **1986**, *84*, 6170.
(31) Varandas, A. J. C. *J. Mol. Struct. (Theochem)* **1988**, *166*, 59.
(32) Davidsson, J.; Nyman, G. *Chem. Phys.* **1988**, *125*, 171.
(33) Miller, J. A. *J. Chem. Phys.* **1981**, *74*, 5120.
(34) Clary, D. C.; Werner, H.-J. *Chem. Phys. Lett.* **1984**, *112*, 346.
(35) Troe, J. *J. Phys. Chem.* **1986**, *90*, 3485.
(36) Murrell, J. N.; Hassani, N. M. R.; Hudson, B. *Mol. Phys.* **1987**, *60*, 1343.
(37) Varandas, A. J. C. *Faraday Discuss. Chem. Soc.* **1987**, *84*, 353.
(38) Varandas, A. J. C., to be published.
(39) Foner, S. N.; Hudson, R. L. *J. Chem. Phys.* **1953**, *21*, 1608.
(40) Ingold, K. U.; Bryce, W. A. *J. Chem. Phys.* **1956**, *24*, 360.
(41) Foner, S. N.; Hudson, R. L. *J. Chem. Phys.* **1955**, *23*, 1364.
(42) Milligan, D. E.; Jacox, M. E. *J. Chem. Phys.* **1963**, *38*, 2627.
(43) Ogilvie, J. F. *Spectrochim. Acta* **1967**, *23A*, 737.
(44) Jacox, M. E.; Milligan, D. E. *J. Mol. Spectrosc.* **1972**, *42*, 495.
(45) Ogilvie, J. F. *Can. J. Spectrosc.* **1973**, *19*, 171.

0022-3654/90/2094-8073$02.50/0

long-range interactions.[31,32,38]

Recently[87] we reported two new potential energy functions for the HO_2 molecule ($\tilde{X}^2A''$) from the semiempirical DMBE method[97-99] by using the ab initio energies of Melius and Blint[75] as calibration data. They have been denoted DMBE II and DMBE III in the original paper, a notation also followed in the current work; refer to ref 87 for details. As usual, both these DMBE potential energy surfaces are written as a sum of short-range-type and long-range-type contributions, which are in turn written as a sum of two-body and three-body terms; see section 2 and the Appendix. The only difference between these potentials is on the short-range three-body contribution, which has been referred to as the three-body nonelectrostatic energy term, $V^{(3)}_{EHF,nele}$. For the DMBE II potential energy surface, $V^{(3)}_{EHF,nele}$ was chosen to conform with the corresponding term calculated from the ab initio MCSCF energies of Melius and Blint. Although this requirement has also been warranted to some extent in the DMBE III potential energy surface, the emphasis in this case has been to reproduce the quadratic spectroscopic force field of the hydroperoxyl radical. It should be recalled, however, that the Melius–Blint energies do not cover uniformly all important regions of the molecular configuration space, and in some regions the data are even nonexistent.

Since then, accurate ab initio complete-active-space self-consistent field contracted configuration interaction (CASSCF/CCI) calculations of the long-range O + OH interaction potential appeared by Walch et al.[81] covering the regions near the OH···O hydrogen-bonded minimum and the reaction path for the title reaction. These ab initio energies have most recently been corrected semiempirically by the double many-body expansion scaled external correlation (DMBE-SEC) method[88] to account for the excitations beyond singles and doubles, and, most importantly, for the incompleteness of the basis set. As suggested elsewhere,[88] it would be interesting to use these DMBE-SEC energies to recalibrate the HO_2 DMBE III functional form and assess the effect of such recalibration on the dynamics of the O + OH → O_2 + H reaction.

Thus, an important motivation for the present work has been to obtain a new DMBE potential energy surface for $HO_2(\tilde{X}^2A'')$ that uses these more accurate DMBE-SEC ab initio energies for the calibration procedure. For regions of configuration space not covered by the DMBE-SEC data, we have retained some especially chosen points from Melius and Blint; see section 2. Furthermore, to shape the deep minima associated with the stable hydroperoxyl radical, we have imposed that the new potential energy surface should reproduce the most recent estimates for the experimental dissociation energy,[81] equilibrium geometry,[59] and quadratic force constants.[60] At an advanced state of our work, new ab initio CCI electronic structure calculations appeared by Walch and Rohlfing[82] for H–O_2 C_{2v} geometries covering the saddle point region for the H-atom-exchange process. This information has also been included in the current calibration procedure. To conform with previous notation, the potential energy surface reported in this work is hereafter referred to as DMBE IV.

The plan of this paper is as follows. Section 2 reports the procedure used to obtain the current HO_2 DMBE IV potential energy surface. The main features of this new potential function are discussed in section 3. Section 4 reports the results of some exploratory quasiclassical trajectory calculations for the title reaction using this potential energy surface. Although an important motivation for future work is to carry out a detailed dynamics study of the title reaction and its reverse, the calculations reported in section 4 will certainly allow a first judgement of its reliability insofar as the dynamics are concerned. The main conclusions are gathered in section 5.

Unless mentioned otherwise, all quantities are reported in atomic units: 1 bohr (a_0) = 1 au of length = 0.052 917 7 nm; 1 hartree (E_h) = 1 au of energy = 4.359 821 5 aJ.

2. Input Data and Calibration Procedure

In the DMBE method[97-99] the molecular potential is partitioned into an extended-Hartree–Fock-type (EHF) energy and the dynamical correlation (corr) energy, both of which are written in

(46) Smith, D. W.; Andrews, L. *J. Chem. Phys.* **1974**, *60*, 81.
(47) Radford, H. E.; Evenson, K. M.; Howard, C. J. *J. Chem. Phys.* **1974**, *60*, 3178.
(48) Hougen, J. T.; Radford, H. E.; Evenson, K. M.; Howard, C. J. *J. Mol. Spectrosc.* **1975**, *56*, 210.
(49) Beers, Y.; Howard, C. J. *J. Chem. Phys.* **1976**, *64*, 1541.
(50) Tuckett, R. P.; Freedman, P. A.; Jones, W. J. *Mol. Phys.* **1979**, *37*, 379.
(51) Tuckett, R. P.; Freedman, P. A.; Jones, W. J. *Mol. Phys.* **1979**, *37*, 403.
(52) Barnes, C. E.; Brown, J. M. *J. Mol. Spectrosc.* **1980**, *84*, 179.
(53) Howard, C. J. *J. Am. Chem. Soc.* **1980**, *102*, 6937.
(54) Charo, A.; De Lucia, F. C. *J. Mol. Spectrosc.* **1982**, *94*, 426.
(55) Buchanan, J. W.; Thrush, B. D.; Tyndall, G. S. *Chem. Phys. Lett.* **1983**, *103*, 167.
(56) Shum, L. G. S.; Benson, S. W. *J. Phys. Chem.* **1983**, *87*, 3479.
(57) Yamada, C.; Endo, Y.; Hirota, E. *J. Chem. Phys.* **1983**, *78*, 4379.
(58) Saito, S.; Endo, Y.; Hirota, E. *J. Mol. Spectrosc.* **1983**, *98*, 138.
(59) Lubic, K. G.; Amano, T.; Uehara, H.; Kawaguchi, K.; Hirota, E. *J. Chem. Phys.* **1984**, *81*, 4826.
(60) Uehara, H.; Kawaguchi, K.; Hirota, E. *J. Chem. Phys.* **1985**, *83*, 5479.
(61) Lewis, R. S.; Watson, R. T. *J. Phys. Chem.* **1980**, *84*, 3495.
(62) Howard, M. J.; Smith, I. W. M. *J. Chem. Soc., Faraday Trans. 2* **1981**, *77*, 997.
(63) Howard, M. J.; Smith, I. W. M. *Prog. React. Kinet.* **1983**, *12*, 55.
(64) Cohen, N.; Westberg, K. R. *J. Phys. Chem. Ref. Data* **1983**, *12*, 531.
(65) Frank, P.; Just, Th. *Ber. Bunsen-Ges. Phys. Chem.* **1985**, *89*, 181.
(66) Pirraglia, A. N.; Michael, J. V.; Sutherland, J. W.; Klemm, R. B. *J. Phys. Chem.* **1989**, *93*, 282.
(67) Kleinermanns, K.; Wolfrum, J. *J. Chem. Phys.* **1984**, *80*, 1446.
(68) Fujii, N.; Shin, K. S. *Chem. Phys. Lett.* **1988**, *151*, 461.
(69) Kleinermanns, K.; Linnebach, E.; Pohl, M. *J. Chem. Phys.* **1989**, *91*, 2181.
(70) Hall, G. E.; Sears, T. J. *Chem. Phys. Lett.* **1989**, *158*, 184.
(71) Liskow, D. H.; Schaefer III, H. F.; Bender, C. F. *J. Am. Chem. Soc.* **1971**, *93*, 6734.
(72) Gole, J. L.; Hayes, E. F. *J. Chem. Phys.* **1972**, *57*, 360.
(73) Blint, R. J.; Newton, M. D. *J. Chem. Phys.* **1973**, *59*, 6220.
(74) Buenker, R. J.; Peyerimhoff, S. D. *Chem. Phys. Lett.* **1976**, *37*, 208.
(75) Melius, C. F.; Blint, R. J. *Chem. Phys. Lett.* **1979**, *64*, 183.
(76) Langhoff, S. R.; Jaffe, R. L. *J. Chem. Phys.* **1979**, *71*, 1475.
(77) Komornicki, A.; Jaffe, R. L. *J. Chem. Phys.* **1979**, *71*, 2150.
(78) Dunning, T. H., Jr.; Walch, S. P.; Goodgame, M. M. *J. Chem. Phys.* **1981**, *74*, 3482.
(79) Metz, J.-Y.; Lievin, J. *Theoret. Chim. Acta* **1983**, *62*, 195.
(80) Vazquez, G. J.; Peyerimhoff, S. D.; Buenker, R. J. *Chem. Phys.* **1985**, *99*, 239.
(81) Walch, S. P.; Rohlfing, C. M.; Melius, C. F.; Bauschlicher, C. W., Jr. *J. Chem. Phys.* **1988**, *88*, 6273.
(82) Walch, S. P.; Rohlfing, C. M. *J. Chem. Phys.* **1989**, *91*, 2373.
(83) Farantos, S.; Leisegang, E. C.; Murrell, J. N.; Sorbie, K.; Teixeira-Dias, J. J. C.; Varandas, A. J. C. *Mol. Phys.* **1977**, *34*, 947.
(84) Gauss, A., Jr. *J. Chem. Phys.* **1978**, *68*, 1689.
(85) Varandas, A. J. C.; Brandão, J. *Mol. Phys.* **1986**, *57*, 387.
(86) Lemon, W. J.; Hase, W. L. *J. Phys. Chem.* **1987**, *91*, 1596.
(87) Varandas, A. J. C.; Brandão, J.; Quintales, L. A. M. *J. Phys. Chem.* **1988**, *92*, 3732.
(88) Varandas, A. J. C. *J. Chem. Phys.* **1989**, *90*, 4379.
(89) Miller, J. A. *J. Chem. Phys.* **1981**, *75*, 5349.
(90) Miller, J. A.; Brown, N. J. *J. Phys. Chem.* **1982**, *86*, 772.
(91) Kleinermanns, K.; Schinke, R. *J. Chem. Phys.* **1984**, *80*, 1440.
(92) Quintales, L. A. M.; Varandas, A. J. C.; Alvariño, J. M. *J. Phys. Chem.* **1988**, *92*, 4552.
(93) Markovic, N.; Nyman, G.; Nordholm, S. *Chem. Phys. Lett.* **1989**, *159*, 435.
(94) Rai, S. N.; Truhlar, D. G. *J. Chem. Phys.* **1983**, *79*, 6046.
(95) Song, K.; Chesnavich, W. J. *J. Chem. Phys.* **1989**, *91*, 4664.
(96) Spnoholtz, B.; Truong, T. N.; Varandas, A. J. C.; Truhlar, D. G., to be published.
(97) Varandas, A. J. C. *J. Mol. Struct. (Theochem)* **1985**, *120*, 401.
(98) Varandas, A. J. C. In *Structure and Dynamics of Weakly Bound Molecular Complexes*; Weber, A., Ed.; D. Reidel: Dordrecht, 1987; p 357.
(99) Varandas, A. J. C. *Adv. Chem. Phys.* **1988**, *74*, 255.

the form of a cluster expansion usually referrred to as the many-body expansion.[100] The basic methodology has been described in detail in previous publications, and we therefore outline in the Appendix only the mathematical formulas necessary for the current work (for more details see ref 87).

All terms in the current HO_2 DMBE IV potential energy surface have functional forms similar to those previously used[87] with the exception of the three-body nonelectrostatic EHF term ($V^{(3)}_{EHF,nele}$) in which the pre-tanh polynomial is now of order 6. This modification has been found convenient to achieve chemical accuracy (≈1.0 kcal mol^{-1}) in the least-squares fit to the DMBE-SEC energies, while keeping enough flexibility to reproduce also the experimental spectroscopic force field of the hydroperoxyl radical. More specifically, the new polynomial form in eq A6 contains all terms in Q_1, Q_2, and Q_3 (see eq A8) having the appropriate permutational symmetry up to sixth order rather than up to fifth order.[87]

The strategy employed for the parametrization of $V^{(3)}_{EHF,nele}$, eq A6, is also similar to that previously used for the DMBE III potential energy surface, and we summarize next only the basic methodology. First, for a given triatomic geometry, we remove the sum of the two-body energy terms from the corresponding ab initio DMBE-SEC interaction energy (this is defined with respect to the infinitely separated ground-state atoms). Then one also subtracts the three-body electrostatic ($V^{(3)}_{ele}$; eq A9) and dynamical correlation ($V^{(3)}_{corr}$; eq A10) energy contributions from the total three-body energy calculated in that way. It is the remaining energy so obtained (this corresponds to the three-body nonelectrostatic extended-Hartree–Fock energy previously[87] denoted as $V^{(3)}_{EHF'}$) that we adjust to the three-body polynomial form of eq A6. A corresponding procedure is adopted for the gradients and curvatures used for the least-squares fitting procedure, as we describe below.

To keep the numerical difficulties at a minimum level, the nonlinear parameters $\gamma_1^{(i)}$ (i = 1–3) have been constrained to have the values reported in ref 87. Note the slightly different values used for $\gamma_0^{(i)}$, which is due to the relation $\gamma_0^{(i)} = -\gamma_1^{(i)} R_i^{ref}$ and the fact that we have adopted a somewhat different equilibrium geometry for the triatomic. We recall that R_i^{ref} (i = 1–3) is a reference C_{2v} geometry defined as $R_1^{ref} = R_1^e$ and $R_2^{ref} = R_3^{ref} = (R_2^e + R_3^e)/2$, where R_i^e (i = 1–3) are the three equilibrium HO_2 bond distances.

As referred to above, the set of input least-squares ab initio points consisted of all tabulated DMBE-SEC energies[88] (except those involving geometries for which one bond distance is equal to 50.0a_0) and 203 points from the work of Melius and Blint[75] especially chosen to guide the fit at regions uncovered by the DMBE-SEC data. Also included in the least-squares data set are six CCI + Q ab initio energies most recently reported by Walch and Rohlfing[82] for H–O_2 C_{2v} geometries, namely, the first two points and the last four points in Tables II and III of their work, respectively. The remaining points in those tables were discarded as they referred to geometries very close to the C_{2v} intersection of the $^2A_2$ and $^2B_1$ electronic states. We note that, in comparison to the work by Walch et al., the calculations by Walch and Rohlfing use a different one-particle hydrogen-atom basis set, which appears to intrpduce smaller errors in the computed HO_2 energies. Although the Walch–Rohlfing results could, in principle, be made consistent with those reported in ref 88 by using the DMBE-SEC method, this approach has not been followed due to the unavailability, at the time the current work was completed, of OH CASSCF and CASSCF/CCI potential energy curves (and eventually CASSCF and CASSCF/CCI energies for equilibrium HO_2) calculated by using the new hydrogen atom basis set. Accordingly, the six Walch–Rohlfing selected energies have not been scaled by using the DMBE-SEC method but include instead the Davidson's[101] correction for quadruple excitations (CCI + Q). The three different sets of input ab initio energies[75,82,88] (in addition to the experimental data described in the next paragraph) have been merged together in the same global fitting procedure by attributing them different least-squares weights according to the estimated reliability, number of points, and region of molecular configuration space. The criteria for data selection are described in Table I, while the corresponding least-squares weights used for the fitting procedure are defined in Table II.

Treated on the same least-squares footing (see ref 87) and carrying the special weights also defined in Table II are the experimental HO_2 well depth (this is chosen as the experimental value tabulated by Walch et al.[81]) and the complete quadratic force field[60,100] at the equilibrium HO_2 geometry.[59] More specifically, we have forced the potential energy function to satisfy the requirement of having zero first derivatives at the minimum in addition to reproduce the experimental spectroscopic force constants (F_{ij}) for HO_2. For the diagonal force constants F_{ii} (i = 1, 2, α; α is the ∠HOO angle) and the mixed $F_{1\alpha}$ term, we used as input data the most recent estimates of Uehara et al.,[60] who assumed the remaining mixed force constants (F_{12} and $F_{2\alpha}$) equal to zero. Rather than making this assumption, we have instead chosen to complete the quadratic force field by using Ogilvie's[45] F_{12} and $F_{2\alpha}$ force constants reported in ref 100. The greater uncertainty in their values is somewhat reflected on the least-squares weights, which have been chosen to be smaller for F_{12} and $F_{2\alpha}$.

The criteria for weight selection deserves some further comment though. Because the Melius–Blint points referred to in Table I were mainly used to guide the fitted functional form at the regions not covered by the DMBE-SEC energies, they have carried a (reference) least-squares weight of 1; all other Melius–Blint points not referred to explicitly in this work were therefore given a weight of 0, i.e., they have been discarded. All DMBE-SEC points were then given a least-squares weight of 100. Yet, to improve further the quality of the fit at large interatomic separations, we found it convenient to assign a weight of 10000 to the (DMBE-SEC and CCI + Q) points having at least one bond distance greater than or equal to 5.0a_0. Similarly, emphasis was given to the six CCI + Q ab initio points of Walch and Rohlfing which carried

TABLE I: Selected ab Initio Points Used for the Calibration of the Current HO_2 DMBE IV Potential Energy Surface

ref	criteria
DMBE-SEC[88]	all points[a]
Melius–Blint[b,75]	∠HOO ≥ 130°
	$R_{OH} < 1.73a_0$
	(∠HOO ≤ 75°) ∧ ($R_{OO} \le 3.0a_0$)
	(∠HOO = 90°) ∧ ($R_{OO} = 2.30a_0$)
Walch–Rohlfing[82]	($R_{H\text{-}OO} < 2.5a_0$) ∨ ($R_{H\text{-}OO} > 3.5a_0$)

[a] See text. [b] An additional criterion for the selection of the Melius–Blint points has been[85] $R_1 + R_2 + R_3 \le 12.0a_0$.

TABLE II: Number of Points and Weights Used for the Least-Squares Fitting Procedure of the Three-Body Nonelectrostatic Extended-Hartree–Fock-Type Energy Term (Eq A6)[a]

ref	criteria	no.	wt
DMBE-SEC[88]	general	63	100
	R_1, R_2 or $R_3 \ge 5.0a_0$	89	10000
Melius–Blint[75]	general	182	1
	∠HOO = 180°	12	10
	near the C_{2v} saddle point[b]	9	1000
Walch–Rohlfing[82]	general	5	1000
	R_1, R_2, or $R_3 \ge 5.0a_0$	1	10000
expt			
refs 59, 81	equilibrium geom	1	100000
	first partial derivatives	3	100000
ref 60	F_{11}, F_{22}, $F_{\alpha\alpha}$, and $F_{1\alpha}$	4	$1000/F_{ij}^2$
refs 45, 100	F_{12}, $F_{2\alpha}$	2	$1/F_{ij}^2$

[a] R_1 labels the OO distance. [b] For completeness, their bond lengths (R_1, R_2), in a_0, for an included angle ∠HOO of 60°, are reported here: (2.50, 2.50), (2.70, 2.50), (2.70, 3.00), (2.80, 1.95), (2.90, 1.88), (3.00, 1.50), (3.00, 2.00), (3.00, 2.50), and (3.00, 3.00).

(100) Murrell, J. N.; Carter, S.; Farantos, S. C.; Huxley, P.; Varandas, A. J. C. *Molecular Potential Energy Functions*; Wiley: Chichester, 1984.
(101) Langhoff, S. R.; Davidson, E. R. *Int. J. Quantum Chem.* **1974**, *8*, 61.

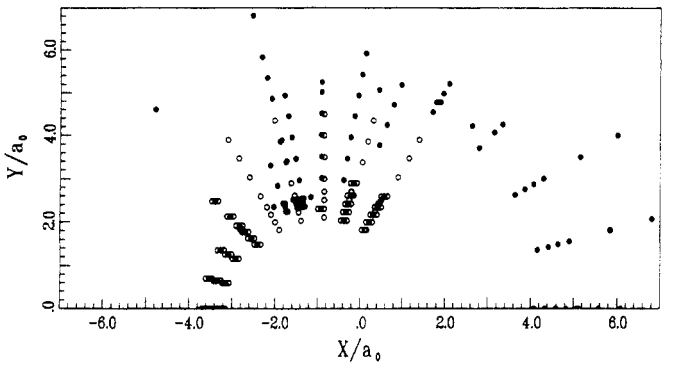

Figure 1. Illustrative distribution of the input least-squares ab initio energies for an O atom moving around an OH molecule, the bond length of which is allowed to relax between $1.6344a_0$ and $2.0344a_0$: ●, DMBE-SEC;[88] ○, Melius-Blint.[75]

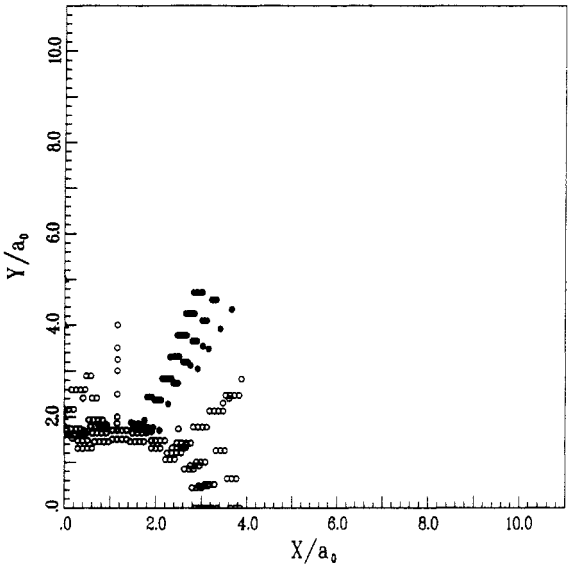

Figure 2. Illustrative distribution of the input ab initio energies for a H atom moving around an O_2 molecule, the bond distance of which is allowed to relax between $1.6818a_0$ and $2.8818a_0$: ●, DMBE-SEC;[88] ○, Melius-Blint;[75] ▲, Walch and Rohlfing.[82]

out an especial weight of 1000. Because the latter to not cover C_s geometries close to the saddle point for the H-atom exchange, an especial weight of 1000 was also given to nine selected points from Melius and Blint (for completeness, their geometries are also identified in Table II). A similar reasoning was applied to the 12 Melius-Blint points with $C_{\infty v}$ symmetry, which correspond to ∠HOO = 180°. These carried out a weight of 10 in the least-squares fitting procedure. Figures 1 and 2 illustrate the distribution of the fitted energies and reference sources over the molecule configuration space.

The quality of the current fit may be judged from its root-mean-square error (rms), which is $0.00147E_h$ (0.92 kcal mol^{-1}), $0.0187E_h$ (11.73 kcal mol^{-1}), and $0.00336E_h$ (2.11 kcal mol^{-1}) for the DMBE-SEC, Melius-Blint, and Walch and Rohlfing data sets, respectively. We note that the present fit has achieved chemical accuracy with respect to the DMBE-SEC points, while the rms error for the points of Walch and Rohlfing should be close to the accuracy of their calculations. For the Melius-Blint points, the rms error of the present fit is considerably larger than for the DMBE-SEC and Walch-Rohlfing energies but only about 4 kcal mol^{-1} higher than the value achieved in our previous DMBE III potential energy surface.

We conclude this section by noting that unlike previous calibrations for the DMBE II and III potential energy surfaces, no arbitrary points were found necessary to successfully complete the current least-squares fit. This may be attributed to the more uniform distribution of the ab initio data over the molecular configuration space.

TABLE III: Coefficients for the Three-Body Nonelectrostatic Extended-Hartree-Fock-Type Energy Term (Eq A6)[a,b]

V_0 = 4.540 572 9

c_1 = 1.080 054 1	c_{18} = −4.018 841 4 (−1)	c_{34} = −1.071 441 0 (−3)
c_2 = −5.183 093 4	c_{19} = −6.270 611 0 (−2)	c_{35} = 2.631 642 9 (−3)
c_3 = −1.910 512 6	c_{20} = 1.124 010 3 (−1)	c_{36} = 4.715 220 9 (−3)
c_4 = 1.113 423 2	c_{21} = 4.211 821 6 (−2)	c_{37} = −4.541 411 0 (−4)
c_5 = 5.349 529 8	c_{22} = 2.441 897 0 (−2)	c_{38} = 6.646 097 1 (−3)
c_6 = −1.105 786 1	c_{23} = −4.402 634 2 (−2)	c_{39} = 6.140 258 5 (−3)
c_7 = 9.457 242 9 (−1)	c_{24} = −8.227 194 9 (−2)	c_{40} = 1.948 183 9 (−3)
c_8 = −9.222 358 7 (−1)	c_{25} = 1.016 216 3 (−2)	c_{41} = 2.893 337 5 (−3)
c_9 = 2.964 687 3 (−2)	c_{26} = −4.529 292 0 (−2)	c_{42} = −5.441 079 8 (−3)
c_{10} = −2.282 858 2	c_{27} = −5.949 901 9 (−2)	c_{43} = −6.846 248 2 (−3)
c_{11} = 1.028 333 3	c_{28} = 7.506 823 9 (−2)	c_{44} = 7.558 045 6 (−4)
c_{12} = −3.247 858 4 (−1)	c_{29} = 6.237 354 4 (−2)	c_{45} = 1.158 309 3 (−2)
c_{13} = −2.181 771 4 (−1)	c_{30} = −2.545 599 8 (−2)	c_{46} = 1.750 896 1 (−2)
c_{14} = 2.942 027 1 (−1)	c_{31} = −6.485 720 3 (−2)	c_{47} = −1.757 095 8 (−3)
c_{15} = 2.972 142 8 (−1)	c_{32} = −1.165 766 7 (−1)	c_{48} = 6.863 577 7 (−3)
c_{16} = −4.080 915 9 (−2)	c_{33} = 1.280 885 1 (−2)	c_{49} = −6.329 068 7 (−3)
c_{17} = 5.091 806 3 (−1)		
$\gamma_0^{(1)}$ = −2.469 085 3	$\gamma_0^{(2)}$ = −1.641 081 5	$\gamma_0^{(3)}$ = −1.641 081 5
$\gamma_1^{(1)}$ = 9.820 169 8 (−1)	$\gamma_1^{(2)}$ = 6.200 000 0 (−1)	$\gamma_1^{(3)}$ = 6.200 000 0 (−1)

[a] All values are in atomic units. [b] Given in parentheses are the powers of 10 by which the numbers should be multiplied, e.g., 9.457 242 9 (−1) = $9.457\,242\,9 \times 10^{-1}$.

TABLE IV: Coefficients Used for the Ground-State O_2 and OH Potentials (Eqs A2, A3, and A4)[a]

coeff	O_2	OH	coeff	O_2	OH
$-D$	0.142 91	0.138 25	R_0	5.661 69	6.294 89
a_1	3.644 59	2.656 48	R_m	2.281 8	1.8344
a_2	3.928 12	1.745 05	C_6	15.40	10.00
a_3	2.098 67	0.710 14	C_8	235.22	180.45
γ	3.352 25	2.545 33	C_{10}	4066.24	3685.26
α	0	0			

[a] Units are as in Table III.

TABLE V: Coefficients for the Three-Body Electrostatic and Correlation Energy Terms (Eqs A9, A10, and A11)[a,b]

coeff	O–O bond	O–H bond
	Electrostatic (Eq A9)[c]	
K_4	0.0	8.831 28 (−2)
$K'_4 = \eta^{(4)}$	3.352 25	2.545 33
K_5	0.0	8.831 28 (−2)
$K'_5 = \eta^{(5)}$	3.352 25	2.545 33
	Correlation (Eq A10)[d]	
k_6	−2.784 78 (−1)	2.465 01 (−2)
$k'_6 = \eta^{(6)}$	9.527 37 (−1)	6.875 80 (−1)
k_8	−4.681 55 (−1)	5.036 96 (−2)
$k'_8 = \eta^{(8)}$	9.414 86 (−1)	8.254 23 (−1)
k_{10}	−1.205 07	6.294 38 (−2)
$k'_{10} = \eta^{(10)}$	7.237 90 (−1)	9.403 52 (−1)
	Auxiliary Reference Geometry (Eq A11)	
R^0	2.2818	1.8344

[a] In all cases $\eta'^{(n)} = 1$, and for the electrostatic term $\xi = 4$. [b] Units and notation are as in Table III. [c] The dipole–quadrupole and quadrupole–quadrupole electrostatic energy coefficients have the values C_4 = −0.929 21 and C_5 = −1.79. [d] The C_n dispersion coefficients assume the corresponding diatomic values.

3. The New HO_2 DMBE Potential Energy Surface

Table III defines numerically the $V^{(3)}_{EHF,nele}$ term, eq A6, of the current DMBE potential energy surface for ground-state HO_2. Although reported elsewhere,[87] we also give for completeness in Tables IV and V the numerical definition of the remaining coefficients for all energy terms appearing in the Appendix. Minor misprints in the original work[87] have also been corrected in the present tabulations.

Figures 3–5 illustrate the main topographical features of the HO_2 DMBE IV potential energy surface. A comparison between the experimental spectroscopic properties of the hydroperoxyl radical[45,59,60,81,100] and the corresponding values predicted from this as well as from the previous DMBE potential energy surfaces

TABLE VI: Spectroscopic Properties of the Hydroperoxyl Radical[a]

property	DMBE-SEC[88]	DMBE II[87]	DMBE III[87]	DMBE IV (this work)	exptl refs 45, 100	exptl refs 59, 60, 81
			Geometry			
R_1/a_0	2.540	2.584	2.512	2.5143	2.512 ± 0.001	2.5143 ± 0.0018
R_2/a_0	1.851	1.870	1.843	1.8345	1.843 ± 0.004	1.8346 ± 0.0040
∠HOO/deg	103.6	103.70	104.02	104.29	104.02 ± 0.24	104.30 ± 0.39
			Dissociation Energy			
D_e/E_h	−0.2790	−0.2797	−0.2745	−0.2790	−0.2747 ± 0.003	−0.2790 ± 0.0010
			Force Constants			
$F_{11}/E_h a_0^{-2}$		0.426	0.375	0.3774	0.375	0.3774
$F_{22}/E_h a_0^{-2}$		0.273	0.417	0.4287	0.418	0.4286
$F_{\alpha\alpha}/E_h$		0.393	0.241	0.2211	0.240	0.2211
$F_{12}/E_h a_0^{-2}$		0.0186	0.0060	0.0063	0.0064	
$F_{1\alpha}/E_h a_0^{-1}$		0.116	0.0482	0.0414	0.0482	0.0414
$F_{2\alpha}/E_h a_0^{-1}$		−0.0202	−0.0600	−0.0621	−0.0607	

[a] Energies relative to the three isolated atoms. R_1 labels the OO distance.

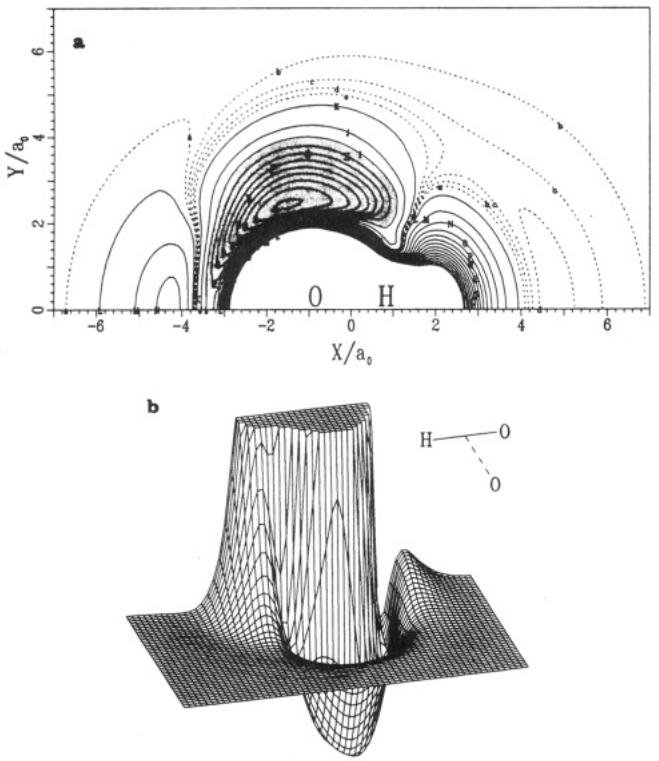

Figure 3. Isoenergy contour plot (a) and corresponding perspective view (b) for an O atom moving around a partially relaxed OH diatomic ($1.6344a_0 \leq R_{OH} \leq 2.0344a_0$), which lies along the X axis with the center of the bond fixed at the origin. Contours in (a) are equally spaced by $0.01E_h$, starting at A = $-0.277E_h$, and dashed lines are equally spaced by $-0.001E_h$, starting at the energy corresponding to the O + OH dissociation limit (a = $-0.17020E_h$). The shaded area represents the regions of configuration space having an energy at least 0.2 eV below the H + O_2 dissociation limit, which are associated to our definition of HO_2* complex for dynamics purposes (see text). Note the absence of an energy barrier for O approaching OH and the metastable minimum associated to the OH···O hydrogen-bonded structure.

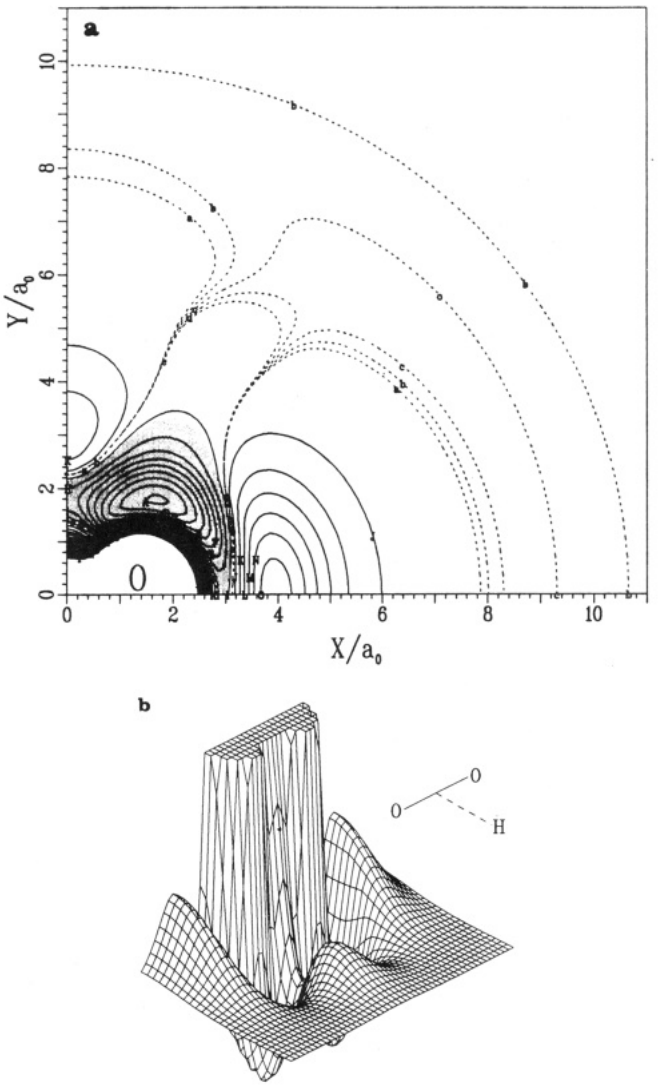

Figure 4. Isoenergy contour plot (a) and perspective view (b) for a H atom moving around a partially relaxed O_2 molecule ($1.6818a_0 \leq R_{OO} \leq 2.8818a_0$) with the center of the bond fixed at the origin. Contours are as in Figure 3, except for dashed contours, which refer now to the H + O_2 dissociation limit (a = $-0.19157E_h$) and are equally spaced by $-0.00002E_h$. Shaded area as in Figure 3. For symmetry reasons we display in (a) only the left half of (b). Note the absence of an energy barrier for H approaching O_2.

is given in Table VI. Table VII compares the geometries and energies of other important stationary points in the current HO_2 DMBE potential energy surface with the ab initio data and other theoretical estimates.

Because the current potential energy surface is topographically similar to previous HO_2 DMBE potentials, we restrict the present analysis to its most important features. Of particular relevance are the entrance and exit channels for the title reaction, which are displayed as isoenergy contour plots and 3D perspective plots in Figures 3 and 4, respectively. By comparison of Figure 3 with Figure 6 of ref 87 and Figure 2 of ref 92 the most notorious difference is the absence of a low-energy $D_{\infty h}$ saddle point for O moving around the H end of OH and of a high-energy barrier separating it from the metastable hydrogen-bonded OH···O minimum ($C_{\infty v}$); see also Figure 5 of this work and Figure 9 of ref 87. In addition, one has a shallower hydrogen-bonded min-

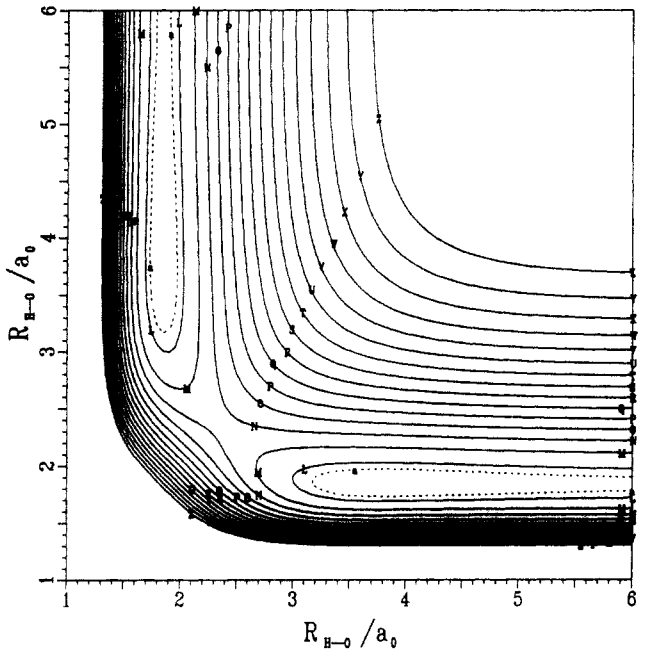

Figure 5. Isoenergy contour plot for the stretching of the two OH bonds in linear OHO. Solid contours are as in Figure 3, and the dashed contour corresponds to the OH dissociation energy ($a = -0.17020E_h$). Note the two equivalent minima associated to the OH···O and O···HO hydrogen-bonded structures.

TABLE VII: Calculated Geometries and Energies of Other Important Stationary Points[a]

property	ab initio	DMBE II[87]	DMBE III[87]	DMBE IV (this work)
	Hydrogen-Bonded OH···O Structure			
R_1/a_0	5.721[b]	5.680	5.808	5.663
R_2/a_0	1.83[b]	1.888	1.863	1.842
R_3/a_0	3.898[b]	3.792	3.945	3.821
∠HOO/deg	0.0[b]	0.0	0.0	0.0
V/E_h	-0.1738[b]	-0.1784	-0.1807	-0.1738
	van der Waals H···O_2 Structure[c]			
R_1/a_0		2.267	2.230	2.282
R_2/a_0		4.824	4.932	7.547
R_3/a_0		4.824	4.932	9.829
∠HOO/deg		76.41	76.94	180.00
V/E_h		-0.2039	-0.2050	-0.1916
	Saddle-Point Structure for the HO_2 Isomerization			
R_1/a_0	2.70[d]	2.783	2.641	2.806
R_2/a_0	2.20[d]	2.212	2.217	2.271
R_3/a_0	2.20[d]	2.212	2.217	2.271
∠HOO/deg	52.19[d]	51.01	53.45	51.85
V/E_h	-0.2120[d]	-0.2332	-0.2509	-0.2141

[a] Energies relative to the three isolated atoms. R_1 labels the OO distance. [b] DMBE-SEC estimate.[88] [c] This structure corresponds to a minimum in the DMBE II and DMBE III potential energy surfaces, although it is a saddle point in the current DMBE surface. [d] CCI + Q estimate.[82]

imum, the properties of which are in excellent agreement with those obtained[88] by fitting a polynomial function to the DMBE-SEC energies; see Table VII. The saddle point connecting the minima associated to the weakly stable hydrogen-bonded minimum and the stable hydroperoxyl radical is seen from Figures 3 and 6 to occur at a C_s geometry defined by $R_{OO} = 5.083a_0$, $R_{OH} = 1.820a_0$, ∠HOO = 40.2°, the energy of which has been calculated to be $V = -0.0026E_h$ (relative to O + OH). Thus, it does not correspond to a true barrier in the sense that it lies below the classical energy for the infinitely separated reactants. As pointed out by Walch et al.,[81] this saddle point results from an avoided intersection between the two different $^2A''$ electronic states corresponding to those minima. Regarding the region of Figure 3 corresponding to an O atom attacking the O end of OH, we simply

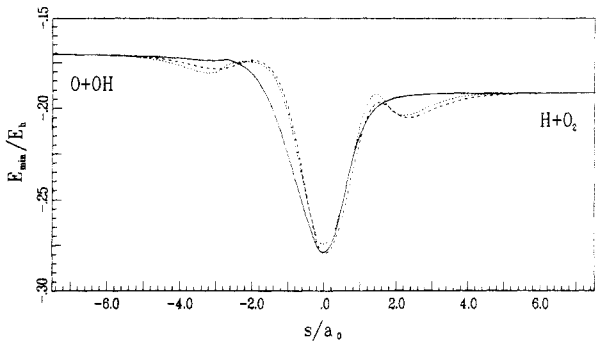

Figure 6. Minimum energy reaction path for the title reaction (s denotes the reaction coordinate). The left-hand side of this Figure corresponds to the O + OH reactants with $-s$ being defined as the distance between the O atom and the center of mass of OH subtracted of its value for the equilibrium HO_2 geometry (i.e., $s = 0$ for this geometry). The right-hand side of this figure shows the corresponding path for the H + O_2 products, s representing now the difference between the distance of the H atom to the center of the O_2 molecule and its value at the equilibrium HO_2 geometry: ---, DMBE II;[87] ---, DMBE III;[87] —, DMBE IV (this work).

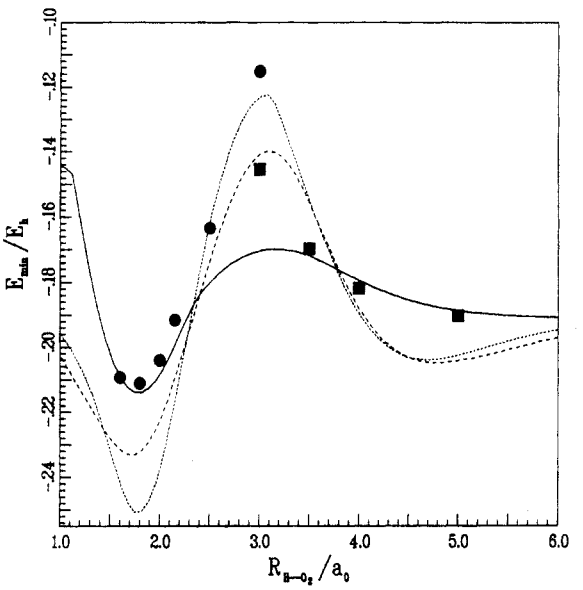

Figure 7. Optimized H + O_2 interaction energy for C_{2v} geometries: ab initio points of Walch and Rohlfing[82] for the $^2A_2$ (●) and $^2B_1$ (■) states; ---, DMBE II;[87] ---, DMBE III;[87] —, DMBE IV (this work).

note that it does not differ qualitatively from that of previous DMBE surfaces. Yet, it is important to emphasize from Figure 1 that the ab initio data do not cover the regions of space where this energy barrier reaches it maximum value. A perspective view of Figure 3a in which the topographical features are highlighted is shown in Figure 3b.

Similarly to Figure 3, we show in Figure 4 energy contours and a perspective view for a H atom moving around a partially optimized O_2 molecule having the center of mass fixed at the origin. The notorious feature in this plot is the absence of an energy barrier for the reverse of the title reaction. Another important feature (which contrasts with ref 87) is the absence of a relatively deep (i.e., a few kcal mol^{-1} deep) van der Waals minimum along the C_{2v} line for H approaching O_2 (see also Figure 7). The existence of a weakly bound T-shaped van der Waals species H···O_2 has been rationalized[85] by analogy with that for HeO_2 and ArO_2 van der Waals molecules. More recently, however, one of us[88] suggested that the presence of strong covalent forces in the case of H approaching O_2 could to some extent invalidate this analogy. Accordingly, in the absence of accurate ab initio calculations it would be difficult to decide whether this metastable minimum was a realistic prediction or an artifact of previous HO_2 DMBE potential energy functions. Because in the present calibration we

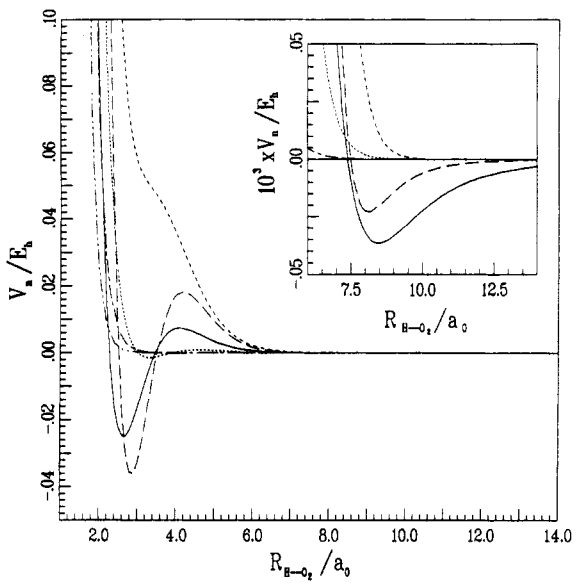

Figure 8. Isotropic (V_0) and anisotropic (V_2, V_4, V_6, V_8, and V_{10}) components of the H–O_2 interaction potential, with the molecule fixed at the equilibrium diatomic geometry. The insert shows a closeup for large distances to illustrate the effect of van der Waals forces: —, V_0; — —, V_2; – – –, V_4; - - -, V_6; – - –, V_8; – – –, V_{10}.

have fitted reasonably well the accurate CCI energies of Walch and Rohlfing (Figure 7), we may believe that such a relatively deep metastable minimum is likely to be absent in the true potential energy surface. Indeed, as shown in Table VII, the van der Waals H···O_2 structure is now a saddle point occurring at a $C_{\infty v}$ structure, which may be rationalized as being due to the larger polarizability of the O_2 molecule along the internuclear axis. This fact becomes clear from the Legendre analysis of the potential energy surface shown in Figure 8. It is seen (see the insert) from this Figure that V_2 is negative for large H–O_2 separations, while it becomes positive at intermediate distances, before returning to negative and again positive with decreasing separations.

Another important attribute of the HO_2 potential energy surface is the C_{2v} saddle point for the HO_2 isomerization. This is well illustrated in Figures 4 and 7. We note that the ab initio points in the latter figure were taken directly from Walch and Rohlfing and may correspond to slightly different values of the optimized O–O bond distance. The sort of agreement between these O–O distances and those predicted from the current HO_2 DMBE potential energy surface is displayed in Table VII for the saddle point corresponding to the H-atom exchange process. Close to this first-order saddle point is a second-order saddle point of C_{2v} geometry ($R_{OO} = 2.304a_0$, $R_{OH} = 3.343a_0$, ∠HOO = 69.8°), which shows as a maximum ($0.0216E_h$ relative to H + O_2) in Figures 4 and 7. This results from the fact that our potential is single-valued, whereas the ab initio potential energy surface corresponds to a crossing of an $^2A_2$ and a $^2B_1$ C_{2v} electronic states. We note that this intersecting C_{2v} locus, for optimal O–O separations, lies near the OH + O dissociation limit in the current DMBE potential energy surface, a result that may have implications in the dynamics of the title reaction.

Figure 5 shows energy contours for the stretching of the two OH bonds in linear OHO. We note that the topography of this region differs from previous DMBE surfaces; see Figure 9 of ref 87. We have now a barrier of about 13.45 kcal mol^{-1} (relative to O + OH) at a $D_{\infty h}$ geometry defined by $R_{OH} = 2.362a_0$. Unfortunately, there are no ab initio estimates that may help us in assessing the reliability of the current potential energy surface in this region. Also seen from this figure are the two asymmetric hydrogen-bonded minima corresponding to the OH···O and O···HO species.

Finally, we show in Figure 6 an approximate minimum energy reaction path obtained by calculating the minimum energy for a given atom–diatom separation. Also shown for comparison in this figure are the equivalent pathways for the HO_2 DMBE II and DMBE III potential energy surfaces. Note that the negative abcissas correspond to O approaching OH, while the positive values correspond to H moving away from O_2. Thus, this coordinate involves a translation by a constant corresponding to the atom–diatom bond distance at the equilibrium HO_2 geometry. Of course, as already pointed out, there are quantitative differences between the current surface and the two previous ones at large atom–diatom separations that stem from the way the various potentials have been calibrated.

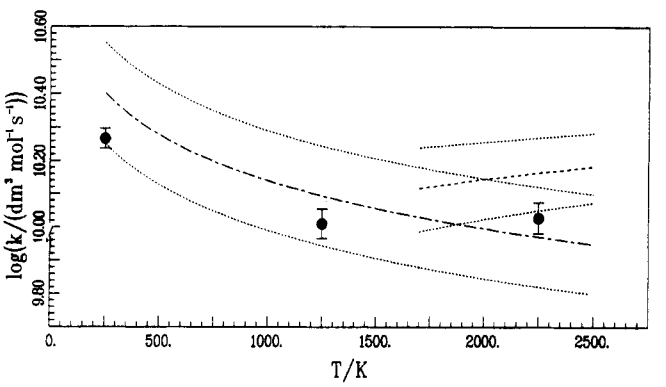

Figure 9. Plot of log [$k(T)$] against T for the title reaction: –·–, Cohen–Westberg[64] (experimental); – – –, Frank–Just[65] (experimental); ●, this work (calculated). The dotted lines represent the uncertainty of the experimental data, while that of the theoretical data is indicated by the error bars; see text.

4. Dynamical Results

In this section, we report the results of preliminary quasiclassical trajectory calculations of the thermal rate coefficient[102] for the title reaction on the HO_2 DMBE IV potential energy surface. The method has been described elsewhere,[92] and the reader is referred to the original work for details.

Figure 9 provides a graphical comparison between the calculated thermal rate coefficients for T = 250, 1250, and 2250 K and the best experimental estimates.[64,65] Only those trajectories that terminated with an energy greater than the zero-point energy of the corresponding diatomic fragment have been counted, all others having been disregarded. The error bars shown in this figure correspond to the 68% confidence intervals and are based on batches of about 1000 trajectories each. The agreement is shown to be good.

If one thinks of the title reaction in terms of the simple chemical model O + OH ⇌ HO_2* → O_2 + H, then we may write

$$k(T) = k_{cap}(T)\, F_{rec}(T) \qquad (1)$$

where $k_{cap}(T)$ is the thermal rate coefficient for forming the complex and $F_{rec}(T) = P_r/P_c$ is a conversion factor for forming H + O_2 products from the HO_2* complexes; P_r is the probability of forming H + O_2, and P_c the probability of complex formation. Note that, following previous work,[92] we define complex as a species whose energy is at least 0.2 eV below that of H + O_2; see the shaded areas in Figures 3 and 4. Note also that the right–left harpoons do not imply chemical equilibrium but emphasize that some trajectories may recross back to reactants after forming the HO_2* complex. For the three temperatures considered here and counting only those recrossed trajectories that terminated with an energy greater than the zero-point energy, the calculated recrossing ratios are 0.83, 0.51, and 0.48, respectively, for T = 250, 1250, and 2250 K. These recrossing ratios can be described within the associated error limits by the form[38]

$$F_{rec}(T) = A_\infty + A \exp(-\tilde{\alpha}T) \qquad (2)$$

where $A_\infty = {}^1/_3$ and $A = {}^2/_3$ are parameters determined from simple statistical arguments and $\tilde{\alpha} \simeq 0.00095$ K^{-1} is a least-squares

(102) Truhlar, D. G.; Muckerman, J. T. *Atom–Molecule Collision Theory*; Bernstein, R. B., Ed.; Plenum: New York, 1981; p 475.

parameter. It is hoped that a more detailed analysis of the dynamics for the title reaction will be presented elsewhere.

5. Concluding Remarks

The DMBE IV potential energy surface described in the current work has been shown to provide a good representation of the most recent and accurate ab initio and experimental data reported for the HO_2 system, while giving the proper R^{-n} long-range behavior at all asymptotic channels.

The results from quasiclassical trajectory calculations of $k(T)$ versus T have also been shown to be in good agreement with experiment over the complete range of temperatures covered by the latter. Corroborating previous results,[30,92] nonstatistical recrossing effects have also been shown to be significant, and hence they should be taken into account in any application of dynamical or statistical theories to the title reaction.

After this work was completed, two preprints by Graff and Wagner[103] and Wagner and Graff[104] came to our attention. The former reports a detailed theoretical study of fine-structure effects on the long-range electrostatic forces and reactivity of $O(^3P) + OH(^2\Pi)$. In particular, the adiabaticity of the title reaction has been analyzed and the half-collision found to be predominantly adiabatic for the state correlating to reaction. This result supports the dynamics approach used in the current study, which includes this effect in the thermal rate constant through a simple multiplicative factor giving the probability of initiating a collision on the reactive surface. Reaction cross sections and rate constants are also reported by using an adiabatic-capture quantum theory and the quantum-mechanical long-range electrostatic potential energy surfaces reported by those authors. Of particular interest to us here is the analysis by Wagner and Graff[104] of our classical optimized-Q (Q = O-atom quadrupole) model[87] for the electrostatic interaction between the quadrupole moment of the O atom and the dipole and quadrupole moments of the OH molecule. We recall that this model assumes that the O-atom quadrupole moment should be optimized at every point of the HO_2 potential energy surface such as to minimize the interaction electrostatic energy; for details, see ref 87. Despite some differences (typically smaller than 0.2 kcal mol^{-1} for O–OH separations greater than $5a_0$), Graff and Wagner concluded that they should have rather minor consequences on the dynamics of the title reaction. Because the form of the O–OH long-range electrostatic energy remained unchanged with respect to our previous forms[87] and the calibration procedure (particularly, for regions of the potential energy surface where orbital overlap effects cannot be neglected) was based on the more recent and accurate DMBE-SEC ab initio energies, we may have additional confidence on the reliability of the current HO_2 DMBE potential energy surface.

Acknowledgment. We gratefully acknowledge Drs. M. A. Graff and A. F. Wagner for communicating their work prior to publication. The financial support from the Instituto Nacional de Investigação Científica (INIC), Lisbon, Portugal, is also gratefully acknowledged. M.R.P. also thanks the Ministerio de Educación y Ciencia (Spain) for a postdoctoral fellowship and the Universidad de Valladolid (Spain) for leave of absence.

Appendix

Here we give the basic mathematical formulas for the current HO_2 DMBE IV potential energy surface. Unless mentioned otherwise, all symbols have the meaning previously[87] assigned. For the numerical values, see Tables III–V.

The potential is written as

$$V = \sum_{i=1}^{3}[V^{(2)}_{EHF,i}(R_i) + V^{(2)}_{corr,i}(R_i)] + V^{(3)}_{EHF}(\mathbf{R}) + V^{(3)}_{corr}(\mathbf{R}) \quad (A1)$$

where, as usual, $\mathbf{R} = (R_1,R_2,R_3)$ is a collective variable of the internuclear separations, and the superscripts (2) and (3) denote the two-body and three-body energy terms, respectively. The former assume the form

$$V^{(2)}_{EHF} = DR^{\alpha}(1 + \sum_{i=1}^{3}a_i r^i)\exp(-\gamma r) \qquad r = R - R_m \quad (A2)$$

$$V^{(2)}_{corr} = -\sum_{n=6,8,10} C_n \chi_n(R) R^{-n} \quad (A3)$$

being the dispersion damping functions defined by

$$\chi_n = \{1 - \exp[-(A_n R/\rho) - (B_n R^2/\rho^2)]\}^n$$
$$A_n = \alpha_0 n^{-\alpha_1}$$
$$B_n = \beta_0 \exp(-\beta_1 n) \quad (A4)$$
$$\rho = (R_m + 2.5R_0)/2$$
$$R_0 = 2(\langle r_X^2\rangle^{1/2} + \langle r_Y^2\rangle^{1/2})$$

where α_0, α_1, β_0, and β_1 are universal parameters for any spherical interaction with values 25.9528, 1.1868, 15.7381, and 0.097 29, respectively.

The three-body energy terms are in turn written as

$$V^{(3)}_{EHF} = V^{(3)}_{EHF,nele}(\mathbf{R}) + V^{(3)}_{ele}(\mathbf{R}) \quad (A5)$$

with the three-body nonelectrostatic extended-Hartree–Fock-type energy being defined by

$$V^{(3)}_{EHF,nele} = V^0(1 + c_1Q_1 + c_2Q_3 + c_3{Q_1}^2 + c_4{S_{2a}}^2 + c_5Q_1Q_3 + c_6{S_{2b}}^2 + c_7{Q_1}^3 + c_8Q_1{S_{2a}}^2 + c_9{S_3}^3 + c_{10}{Q_1}^2Q_3 + c_{11}Q_1{S_{2b}}^2 + c_{12}Q_3{S_{2a}}^2 + c_{13}{Q_1}^4 + c_{14}{Q_1}^2{S_{2a}}^2 + c_{15}{S_{2a}}^4 + c_{16}Q_1{S_3}^3 + c_{17}{Q_1}^3Q_3 + c_{18}{Q_1}^2{S_{2b}}^2 + c_{19}Q_1Q_3{S_{2a}}^2 + c_{20}Q_3{S_3}^3 + c_{21}{S_{2a}}^2{S_{2b}}^2 + c_{22}{Q_1}^5 + c_{23}{Q_1}^3{S_{2a}}^2 + c_{24}Q_1{S_{2a}}^4 + c_{25}{Q_1}^2{S_3}^3 + c_{26}{S_{2a}}^2{S_3}^3 + c_{27}{Q_1}^4Q_3 + c_{28}{Q_1}^3{S_{2b}}^2 + c_{29}{Q_1}^2Q_3{S_{2a}}^2 + c_{30}Q_1Q_3{S_3}^3 + c_{31}Q_1{S_{2a}}^2{S_{2b}}^2 + c_{32}Q_3{S_{2a}}^4 + c_{33}{S_{2b}}^2{S_3}^3 + c_{34}{Q_1}^6 + c_{35}{Q_1}^4{S_{2a}}^2 + c_{36}{Q_1}^2{S_{2a}}^4 + c_{37}{Q_1}^3{S_3}^3 + c_{38}Q_1{S_{2a}}^2{S_3}^3 + c_{39}{S_{2a}}^6 + c_{40}{S_3}^6 + c_{41}{Q_1}^5Q_3 + c_{42}{Q_1}^4{S_{2b}}^2 + c_{43}{Q_1}^3Q_3{S_{2a}}^2 + c_{44}{Q_1}^2Q_3{S_3}^3 + c_{45}{Q_1}^2{S_{2a}}^2{S_{2b}}^2 + c_{46}Q_1Q_3{S_{2a}}^4 + c_{47}Q_1{S_{2b}}^2{S_3}^3 + c_{48}Q_3{S_{2a}}^2{S_3}^3 + c_{49}{S_{2a}}^4{S_{2b}}^2)\prod_{i=1}^{3}[1 - \tanh(\gamma_0^{(i)} - \gamma_1^{(i)}R_i)] \quad (A6)$$

where

$$S_{2a}{}^2 = Q_2{}^2 + Q_3{}^2$$
$$S_{2b}{}^2 = Q_2{}^2 - Q_3{}^2$$
$$S_3{}^3 = Q_3{}^3 - 3Q_2{}^2Q_3 \quad (A7)$$

and $Q_i (i=1-3)$ are the usual D_{3h} symmetry coordinates, which are defined in matrix form by

$$\begin{bmatrix} Q_1 \\ Q_2 \\ Q_3 \end{bmatrix} = \begin{bmatrix} \sqrt{1/3} & \sqrt{1/3} & \sqrt{1/3} \\ 0 & \sqrt{1/2} & -\sqrt{1/2} \\ \sqrt{2/3} & -\sqrt{1/6} & -\sqrt{1/6} \end{bmatrix} \begin{bmatrix} R_1 \\ R_2 \\ R_3 \end{bmatrix} \quad (A8)$$

Finally, the three-body electrostatic (ele) and correlation energy (corr) terms have, respectively, the form

$$V^{(3)}_{ele} = \tfrac{1}{2}\sum_{i=1}^{3}\sum_{n=4,5}[C_nG_n(R_{i+1(\mathrm{mod}\,3)})\,h_n(R_{i+2(\mathrm{mod}\,3)}) + C'_nG_n(R_{i+2(\mathrm{mod}\,3)})\,h_n(R_{i+1(\mathrm{mod}\,3)})]\chi_n(R_i)R_i^{-n} \quad (A9)$$

$$V^{(3)}_{corr} = \sum_{i=1}^{3}\sum_{n=6,8,10} C_n\chi_n(R_i)\{1 - \tfrac{1}{2}[g_n(R_{i+1(\mathrm{mod}\,3)})\,h_n(R_{i+2(\mathrm{mod}\,3)}) + g_n(R_{i+2(\mathrm{mod}\,3)})\,h_n(R_{i+1(\mathrm{mod}\,3)})]\}R_i^{-n} \quad (A10)$$

where G_n, g_n, and h_n are auxiliary functions defined by

$$G_n = K_nR^{\xi}\exp[-K'_n(R - R^0)]$$
$$g_n = 1 + k_n\exp[-k'_n(R - R^0)]$$
$$h_n = [\tanh(\eta^{(n)}R)]^{\eta'(n)} \quad (A11)$$

(103) Graff, M. A.; Wagner, A. F., to be published.
(104) Wagner, A. F.; Graff, M. A., to be published.